

## RESEARCH ARTICLE

10.1002/2016JA023473

## Special Section:

Major Results From the MAVEN Mission to Mars

## Key Points:

- MAVEN has observed the first dayside in situ peak electron densities since Viking
- Changes in the peak electron density and peak altitude are well described by Chapman theory
- Changes in electron temperature at the peak altitude are consistent with observed changes in electron density

## Correspondence to:

M. F. Vogt,  
mvogt@bu.edu

## Citation:

Vogt, M. F., et al. (2016), MAVEN observations of dayside peak electron densities in the ionosphere of Mars, *J. Geophys. Res. Space Physics*, 122, doi:10.1002/2016JA023473.

Received 15 SEP 2016

Accepted 11 DEC 2016

Accepted article online 15 DEC 2016

## MAVEN observations of dayside peak electron densities in the ionosphere of Mars

Marissa F. Vogt<sup>1</sup> , Paul Withers<sup>1,2</sup> , Kathryn Fallows<sup>1</sup> , Laila Andersson<sup>3</sup> , Zachary Girazian<sup>4</sup> , Paul R. Mahaffy<sup>4</sup> , Mehdi Benna<sup>4,5</sup> , Meredith K. Elrod<sup>4,6</sup> , John E. P. Connerney<sup>4</sup> , Jared R. Espley<sup>4</sup> , Frank G. Eparvier<sup>3</sup> , and Bruce M. Jakosky<sup>3</sup> <sup>1</sup>Center for Space Physics, Boston University, Boston, Massachusetts, USA, <sup>2</sup>Department of Astronomy, Boston University, Boston, Massachusetts, USA, <sup>3</sup>Laboratory for Atmospheric and Space Physics, University of Colorado Boulder, Boulder, Colorado, USA, <sup>4</sup>NASA Goddard Space Flight Center, Greenbelt, Maryland, USA, <sup>5</sup>CRESST, University of Maryland, Baltimore County, Baltimore County, Maryland, USA, <sup>6</sup>CRESST, University of Maryland, College Park, Maryland, USA

**Abstract** The peak electron density in the dayside Martian ionosphere is a valuable diagnostic of the state of the ionosphere. Its dependence on factors like the solar zenith angle, ionizing solar irradiance, neutral scale height, and electron temperature has been well studied. The Mars Atmosphere and Volatile Evolution spacecraft's September 2015 "deep dip" orbits, in which the orbital periapsis was lowered to ~125 km, provided the first opportunity since Viking to sample in situ a complete dayside electron density profile including the main peak. Here we present peak electron density measurements from 37 deep dip orbits and describe conditions at the altitude of the main peak, including the electron temperature and composition of the ionosphere and neutral atmosphere. We find that the dependence of the peak electron density and the altitude of the main peak on solar zenith angle are well described by analytical photochemical theory. Additionally, we find that the electron temperatures at the main peak display a dependence on solar zenith angle that is consistent with the observed variability in the peak electron density. Several peak density measurements were made in regions of large crustal magnetic field, but there is no clear evidence that the crustal magnetic field strength influences the peak electron density, peak altitude, or electron temperature. Finally, we find that the fractional abundance of O<sub>2</sub><sup>+</sup> and CO<sub>2</sub><sup>+</sup> at the peak altitude is variable but that the two species together consistently represent ~95% of the total ion density.

## 1. Introduction

The ionosphere of Mars is formed by photoionization of atmospheric CO<sub>2</sub> by solar flux at EUV wavelengths. At altitudes below ~180 km the plasma is in photochemical equilibrium and the electron densities are well described by a Chapman layer [Chapman, 1931a, 1931b; Withers, 2009]. The measured electron density profiles feature a main peak that is typically located near ~120–130 km altitude at the subsolar point. This main peak is analogous to the *F* layer at the Earth and is frequently called the *M2* layer [Rishbeth and Mendillo, 2004].

Over the past two decades the Mars Global Surveyor and Mars Express spacecraft have yielded thousands of remote measurements of the peak electron density in the Martian ionosphere. These data, along with complementary modeling studies, have shown how the electron density of the main peak varies spatially and with factors like solar ionizing flux, local magnetic field magnitude and direction, and properties of the neutral atmosphere [e.g., Withers and Mendillo, 2005; Fox and Yeager, 2006; Morgan et al., 2008], making it a valuable single measurement of the state of the Martian ionosphere. However, for nearly 40 years the only in situ observations of the electron density and ion composition at the main peak have come from two profiles measured by the Viking landers [Hanson et al., 1977].

In this paper we report on data from the September 2015 "deep dip" orbits of the Mars Atmosphere and Volatile Evolution (MAVEN) spacecraft at Mars. These data are the first in situ dayside electron density profiles featuring the main peak since the Viking era and the first observations with contemporaneous comprehensive measurements of the local plasma and magnetic field properties. The MAVEN data, which come from 37 orbits over 7 days, provide the first in situ measurements of the electron temperature at the peak and the first opportunity to study variability in properties like the composition of the neutral atmosphere and ionosphere at the main peak.

This paper is organized as follows. Section 2 describes the MAVEN data used in this study. In section 3 we discuss the peak electron density values and their temporal and spatial variability, scale heights calculated from

Chapman function fits to each profile, electron temperatures at the main peak, and the composition of the neutral atmosphere and ionosphere at the main peak. We conclude with a summary.

## 2. Data Used in This Study

For MAVEN's 1 year primary science mission, which began in November 2014, the spacecraft was located in a 4.5 h elliptical orbit around Mars, with periapsis typically at  $\sim 155$  km, apoapsis at  $\sim 6200$  km, and a  $75^\circ$  inclination [Jakosky *et al.*, 2015]. The primary science mission included four deep dip intervals in which periapsis was lowered to  $\sim 120$ – $130$  km for about a week. These deep dip intervals occurred in February, April, July, and September 2015. During the February 2015 deep dip the orbital periapsis was located in the northern hemisphere and near the dawn terminator, with periapsis solar zenith angle (SZA)  $\sim 110^\circ$ . The April 2015 deep dip orbital periapses were located near the subsolar point, at SZA  $\sim 10^\circ$ , and the July 2015 deep dip orbital periapses were located behind the dusk terminator at SZA  $\sim 110^\circ$ . MAVEN observed the main peak, or M2 peak, during the February and July 2015 deep dips but the spacecraft was at nightside solar zenith angles ( $>90^\circ$ ). For the April 2015 deep dip MAVEN did not observe the main peak because the orbital periapsis was  $\sim 130$  km [Ergun *et al.*, 2015] and typical peak altitudes are  $\sim 125$ – $130$  km at  $10^\circ$  solar zenith angle [e.g., Withers, 2009]. Therefore, the September 2015 deep dip interval provided MAVEN's first dayside electron density profiles featuring the main peak and the first measured in situ since the Viking landers. The September 2015 deep dip included 37 orbits, of which only the inbound orbital segments were located on the dayside, and periapsis was located near  $\sim 15:00$  LT in the southern hemisphere at SZA  $\sim 89^\circ$ – $94^\circ$ . Figure 1 shows MAVEN's position during the inbound segments of orbits 1801–1837, which occurred between 2 and 9 September 2015.

MAVEN observations are made in situ, and therefore, the solar zenith angle at which data are collected may change within an orbit depending on the spacecraft trajectory. As a result, the MAVEN electron densities from an individual inbound or outbound orbital pass are not true vertical profiles. Solar zenith angle changes within an individual MAVEN profile can influence the observed peak density and its altitude, especially for observations near  $90^\circ$  SZA. Therefore, in this study we include only the September 2015 deep dip interval and exclude other cases in which MAVEN observed dayside peak densities. MAVEN observed the peak density at  $85^\circ < \text{SZA} < 90^\circ$  in about 36 orbits prior to the September deep dip, but in most of these orbits there was little or no data at dayside solar zenith angles below the main peak so data from these orbits do not provide a full dayside electron density profile. By contrast, in 35 of the 37 September deep dip orbits the peak density was observed at solar zenith angles less than  $85^\circ$ . Therefore, by focusing on the September 2015 deep dip interval we minimize the effects of the changing solar zenith angle over an orbital pass due to MAVEN's trajectory. For the September 2015 deep dip orbits, these effects introduce errors of  $\sim 3$ – $7\%$  in the observed peak density and  $\sim 1$  km in its altitude, as described in more detail in Appendix A.

In this study we use data from MAVEN's Langmuir Probe and Waves (LPW) instrument [Andersson *et al.*, 2015], Neutral Gas and Ion Mass Spectrometer (NGIMS) [Mahaffy *et al.*, 2014], magnetic field investigation (MAG) [Connerney *et al.*, 2015], and Extreme Ultraviolet Monitor (EUVM) [Eparvier *et al.*, 2015]. The LPW measures electron densities between  $\sim 100$   $\text{cm}^{-3}$  and  $10^6$   $\text{cm}^{-3}$  and electron temperatures 500–50,000 K. The data have a 4 s time resolution, which corresponds to  $\sim 1$  km altitude resolution near the peak. NGIMS measures neutral and ion densities with masses from 2 to 150 amu; it does not measure protons [Mahaffy *et al.*, 2014]. We use data from the magnetic field investigation, which includes two magnetometers that measure the magnetic field components with a time resolution of 32 vector samples per second, to examine the effects of crustal magnetic fields on the peak densities. Finally, the EUVM instrument measures the solar irradiance at soft X-ray and EUV wavelengths but is pointed away from the Sun at periapsis. Therefore, to estimate the solar ionizing flux at Mars during this interval we use the EUVM level 3 data product, which is a modeled spectral irradiance based on a modified version of the Flare Irradiance Spectral Model (FISM) [Chamberlin *et al.*, 2007, 2008], called FISM-P, that can be applied to planetary targets other than Earth. The model incorporates measurements from MAVEN's EUVM as well as proxies measured at the Earth that have been adjusted to incorporate the Earth-Sun-Mars angle corresponding to the time of the MAVEN EUVM data. The Earth-based proxies provide measurements of long-term variability produced by the  $\sim 27$  day solar rotation period and 11 year solar cycle, while the MAVEN EUVM measurements are used to constrain daily irradiances and variability produced by solar flares. The modeled irradiances are available with a 1 min time resolution and at wavelengths 0–190 nm. Additional details about the level 3 model data product are given in Eparvier *et al.* [2015].

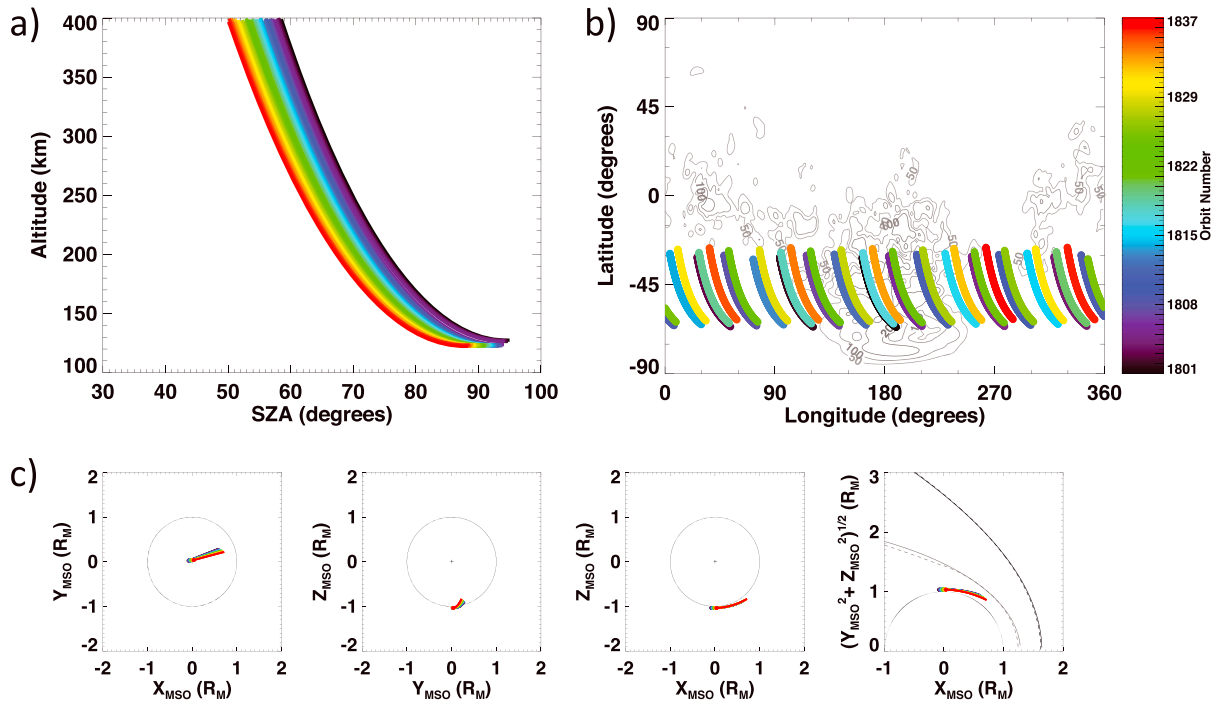


**Figure 1.** MAVEN spacecraft position during the September 2015 deep dip. In all panels color indicates orbit number and the spacecraft position is shown only for the inbound portion of each orbit and at altitudes less than 400 km. (a) Spacecraft altitude as a function of solar zenith angle. (b) Spacecraft latitude as a function of spacecraft longitude. The background shows contours of crustal magnetic field magnitude  $|\beta| = 50, 100,$  and  $200$  nT from the *Cain et al.* [2003] model at 200 km altitude. (c) Position in the MSO coordinate system. The periapsis position is marked by a dot. In the rightmost panel the IMB (gray) and bow shock (black) from *Vignes et al.* [2000] and *Trotignon et al.* [2006] are plotted with solid and dashed lines, respectively.

### 3. Analysis

#### 3.1. Peak Electron Densities: Observations and Variability

Figure 2 presents an overview of the MAVEN observations from orbit 1824 on 6 September 2015, including altitude profiles of the electron density and temperature measured by LPW, ion densities measured by NGIMS, and magnetic field data. The peak electron density, which we refer to as simply the peak density, is  $5.28 \times 10^4 \text{ cm}^{-3}$  and occurs at 136.4 km altitude, which is marked by a horizontal dashed line, and  $81.6^\circ$  solar zenith angle. The electron temperature at the peak altitude is 741.9K; electron temperatures are discussed in more detail in section 3.3. MAVEN did not pass over a region of strong crustal fields during this orbit, and the magnetic field magnitude observed at the peak altitude is 9.78 nT. The NGIMS total ion density, plotted in red in Figure 2a, is qualitatively and quantitatively very similar to the LPW electron density, plotted in black. The peak ion density in the NGIMS profile is  $5.14 \times 10^4 \text{ cm}^{-3}$  and occurs at 140.5 km altitude. The ion composition at the peak is primarily  $\text{O}_2^+$  (~87%), with additional amounts of  $\text{CO}_2^+$  (~8%),  $\text{NO}^+$  (~2%), and  $\text{HNO}^+$  (~2%).

The ionospheric properties from orbit 1824 shown in Figure 2 are typical of the full deep dip data set. Figure 3 shows the variability of the peak density and its altitude over the 37 orbits from the September 2015 deep dip. A summary of the data is listed in Table 1. The peak densities range from  $3.9 \times 10^4 \text{ cm}^{-3}$  to  $6.8 \times 10^4 \text{ cm}^{-3}$ , and the peak altitudes range from 132.1 km to 146.3 km. The peak density steadily increases and the peak altitude steadily decreases over this 7 day interval due to changes in MAVEN's orbital geometry. As shown in Figure 3d, the solar zenith angle at the point when the spacecraft is closest to 140 km ranges from  $86.54^\circ$  for orbit 1801 to  $77.97^\circ$  for orbit 1837.

Analytical photochemical theory, also called Chapman theory, predicts that the dayside peak electron density  $N_m$  and altitude  $z_m$  vary with solar zenith angle according to

$$N_m = N_0 Ch^{-0.5}, \tag{1}$$

$$z_m = z_0 + H \ln Ch, \tag{2}$$

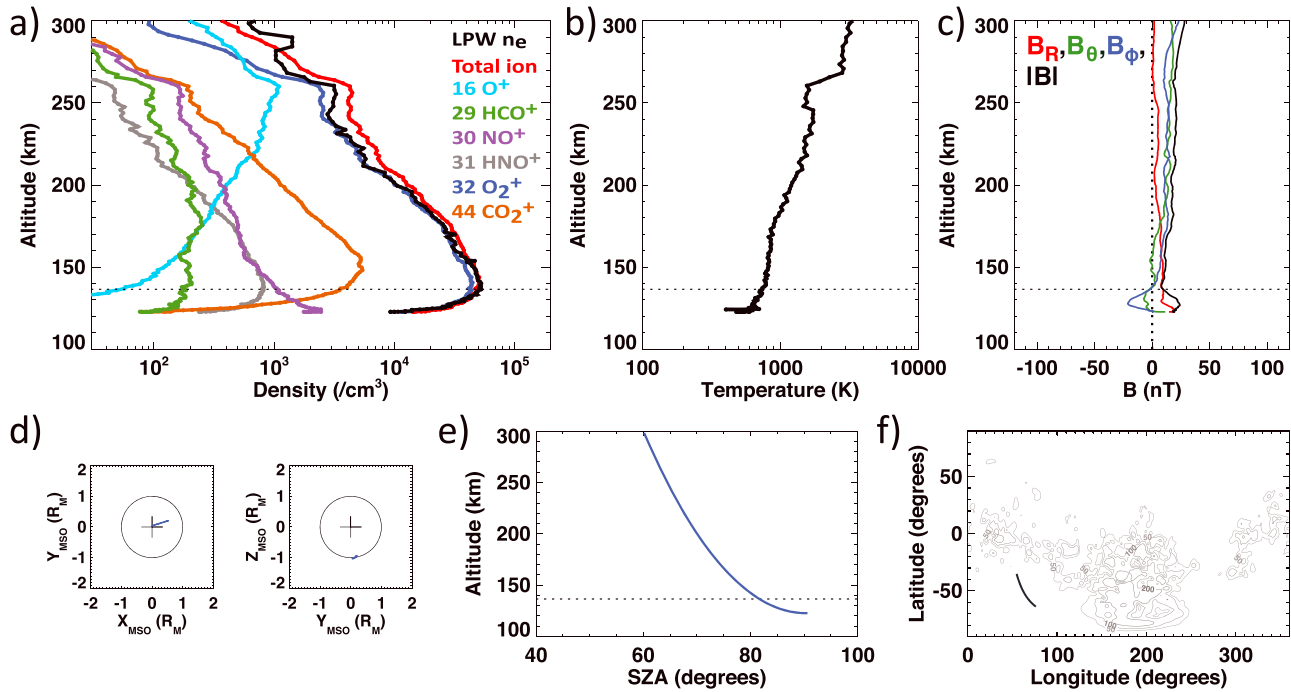


**Figure 2.** MAVEN LPW, NGIMS, and MAG data and spacecraft position from the inbound portion of orbit 1824 on 6 September 2015. (a) Altitude profiles of the LPW electron density (black), NGIMS total ion density (red), and various ion species with masses as noted. (b) Altitude profile of the LPW electron temperature. (c) Altitude profile of the magnetic field components and field magnitude. (d) Spacecraft position in the MSO coordinate system. (e) Spacecraft altitude as a function of solar zenith angle. (f) Spacecraft latitude as a function of longitude. The background shows contours of crustal magnetic field magnitude  $|B| = 50, 100, \text{ and } 200 \text{ nT}$  from the *Cain et al.* [2003] model at 200 km altitude. Data in Figures 2a–2c were collected over about 8 min starting at 13:37. In Figures 2d–2f the spacecraft position is shown only for altitudes less than 300 km. The dashed horizontal line in Figures 2a, 2b, 2c, and 2e indicates the altitude at which the peak electron density was observed, 140.5 km.

where  $N_0$  and  $z_0$  are the subsolar peak density and altitude, respectively, and  $Ch$  is the Chapman grazing function [Chapman, 1931b; Smith and Smith, 1972], which is a function of solar zenith angle and the neutral scale height. For small solar zenith angles the Chapman grazing function can be approximated by  $\sec(\chi)$ , where  $\chi$  is the solar zenith angle. These predictions are valid when planetary curvature can be neglected and ignore the effects of transport processes. The dependence of both the peak density and peak altitude on solar zenith angle is broadly consistent with these predictions, as described in more detail in section 3.2. Therefore, in Figure 3c we plot the inferred subsolar peak density  $N_0$ , which allows us to ignore the effects of the changing orbit geometry over this interval and focus on orbit-to-orbit variability. We calculate  $N_0$  by inverting equation (1), assuming a neutral scale height of 10 km for the Chapman grazing function. The inferred  $N_0$  values range from  $1.15 \times 10^5 \text{ cm}^{-3}$  to  $1.58 \times 10^5 \text{ cm}^{-3}$ .

Previous studies have linked variability in the peak density to factors like proximity to regions of strong crustal magnetic fields or temporal changes in external solar drivers [e.g., Martinis et al., 2003; Nielsen et al., 2007]. However, we do not find a clear association between orbit-to-orbit changes in the peak density and either the presence or absence of large crustal magnetic fields. For example, when MAVEN passed over regions of strong crustal fields it observed both large (e.g., orbit 1817) and small (e.g., orbit 1811) subsolar peak densities, as shown in Figure 3c. We do not find any systematic dependence of the subsolar peak density on either the magnitude or direction (i.e., vertical or horizontal) of the magnetic field. However, as discussed in more detail in section 3.2, near the peak altitude the electron density profiles are smoothest in regions without a strong crustal magnetic field. The additional noise in the profiles from regions of strong crustal field complicates the identification of the peak electron density and may introduce errors in the peak density. These errors could explain the lack of a clear association between peak density and crustal magnetic field strength, particularly since our study includes only 37 data points. However, it is also possible that crustal fields most strongly influence altitudes high above the photochemical region, where field-aligned transport might play a larger role [e.g., Matta et al., 2014].

In addition, we do not find a clear association between orbit-to-orbit changes in the peak density and changes in the solar ionizing flux. Both the solar irradiance and solar wind were steady and quiet over this

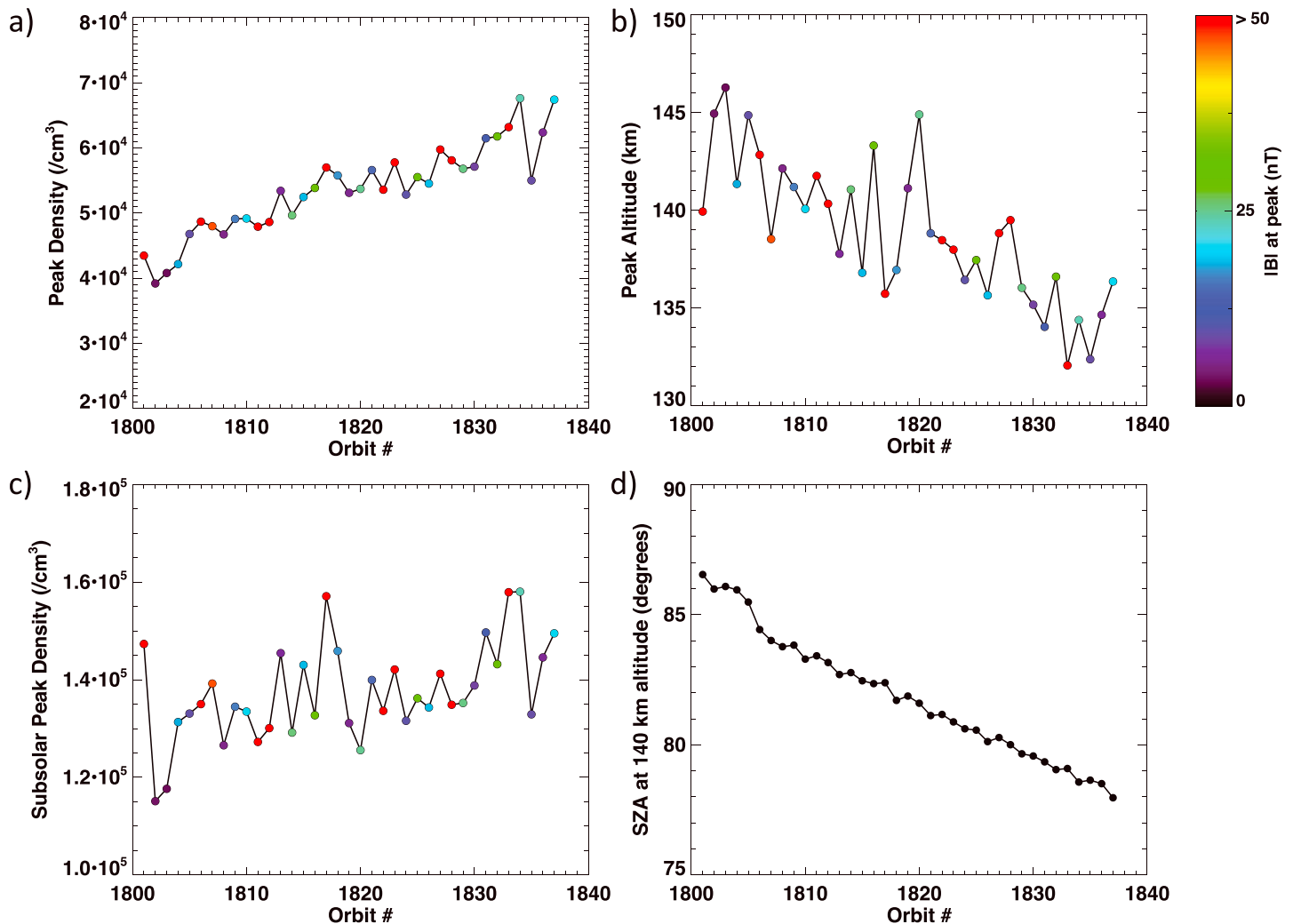


**Figure 3.** Variability of the peak density and altitude observed in during the September 2015 deep dip. (a) Peak density as a function of orbit number. (b) Peak altitude as a function of orbit number. (c) Inferred subsolar peak density as a function of orbit number (see text). (d) Solar zenith angle at  $\sim 140$  km altitude as a function of orbit number. In Figures 3a–3c color indicates the magnetic field magnitude observed at the peak.

7 day interval and therefore cannot explain the observed  $\sim 30\%$  variability in the subsolar peak density. The FISM modeled EUV irradiance at 20–90 nm varied from  $\sim 9.0 \times 10^{-4} \text{ W/m}^2$  to  $\sim 9.3 \times 10^{-4} \text{ W/m}^2$ . Since the subsolar peak density is proportional to the square root of the solar ionizing flux [Withers, 2009], the modeled changes in the EUV irradiance should correspond to changes in the subsolar peak density of  $\sim 2\%$ . MAVEN measurements of energetic protons at periaopsis can be used to compute proxy values for the solar wind velocity and density and therefore also a proxy solar wind dynamic pressure [Halekas et al., 2015, 2016]. This interval featured very quiet solar wind conditions, with an  $\sim 0.6$  nPa proxy solar wind dynamic pressure except for a brief increase to  $\sim 1.5$  nPa from orbits 1810–1815, but those orbits featured typical subsolar peak densities.

### 3.2. Comparison to Previous Data Sets via Analytical Photochemical Theory

Next we consider how well the MAVEN dayside profiles and peak density observations can be described by analytical photochemical theory. Previous studies have shown that electron densities in the Martian ionosphere are well described by Chapman theory in the photochemically controlled region near the main peak ( $< \sim 180$  km). Most studies that have examined electron densities at Mars in the context of Chapman theory have focused on the measured peak density and its altitude [e.g., Fallows et al., 2015, and references therein]. For example, several studies have fit the peak density as a function of solar zenith angle (via the Chapman grazing function) with

**Table 1.** Peak Densities and Peak Altitudes From the September 2015 Deep dip

Orbit Number	Periapsis Date and Time (dd-mm-yyyy/hh:mm:ss)	Periapsis Altitude (km)	SZA at Periapsis (deg)	Peak Density (/cm <sup>3</sup> )	Peak Altitude (km)	SZA at Peak Altitude (deg)	Electron Temperature at Peak Altitude (K)
1801	02-09-2015/04:03:54	127.5	94.47	4.35E + 04	139.9	86.54	771.6
1802	02-09-2015/08:40:48	126.4	94.31	3.92E + 04	145	84.58	776.3
1803	02-09-2015/13:17:34	127.3	94.03	4.08E + 04	146.3	84.3	790.3
1804	02-09-2015/17:54:22	127.3	93.91	4.22E + 04	141.4	85.44	765.5
1805	02-09-2015/22:31:02	126.5	93.72	4.68E + 04	144.9	84.08	790.2
1806	03-09-2015/03:07:37	123.7	93.58	4.87E + 04	142.8	83.66	783.2
1807	03-09-2015/07:44:05	122.8	93.43	4.80E + 04	138.5	84.39	731.7
1808	03-09-2015/12:20:17	122.9	93.2	4.67E + 04	142.1	83.25	756.7
1809	03-09-2015/16:56:27	123.5	93.01	4.91E + 04	141.2	83.44	747.2
1810	03-09-2015/21:32:31	122.4	92.88	4.92E + 04	140.1	83.29	808.3
1811	04-09-2015/02:08:23	123.5	92.63	4.79E + 04	141.8	82.9	822.4
1812	04-09-2015/06:44:16	123.2	92.51	4.86E + 04	140.3	83.03	768.2
1813	04-09-2015/11:19:58	122.5	92.32	5.34E + 04	137.8	83.34	765.5
1814	04-09-2015/15:55:34	123.5	92.14	4.97E + 04	141.1	82.52	767.6
1815	04-09-2015/20:31:06	122.9	91.97	5.25E + 04	136.8	83.37	729.6
1816	05-09-2015/01:06:26	123.2	91.74	5.39E + 04	143.3	81.45	780.2
1817	05-09-2015/05:41:44	123.6	91.53	5.70E + 04	135.7	83.55	749.6
1818	05-09-2015/10:16:56	122.5	91.38	5.58E + 04	137	82.62	750.9
1819	05-09-2015/14:51:57	123.4	91.16	5.31E + 04	141.1	81.48	780
1820	05-09-2015/19:26:57	123.4	91.03	5.37E + 04	144.9	80.3	810.9
1821	06-09-2015/00:01:47	122.5	90.96	5.66E + 04	138.8	81.51	775.9
1822	06-09-2015/04:36:27	123.5	90.62	5.36E + 04	138.5	81.69	775.4
1823	06-09-2015/09:11:05	122.7	90.48	5.78E + 04	138	81.4	757.6
1824	06-09-2015/13:45:31	122.7	90.35	5.28E + 04	136.4	81.66	741.9
1825	06-09-2015/18:19:51	123.4	90.05	5.55E + 04	137.5	81.35	744.3
1826	06-09-2015/22:54:06	122.4	89.88	5.45E + 04	135.7	81.43	728.7
1827	07-09-2015/03:28:14	123.4	89.78	5.98E + 04	138.8	80.54	789
1828	07-09-2015/08:02:18	123.3	89.51	5.81E + 04	139.5	80.14	786.8
1829	07-09-2015/12:36:10	122.4	89.18	5.68E + 04	136	80.71	785
1830	07-09-2015/17:10:02	123.5	89.1	5.71E + 04	135.2	81.15	739.4
1831	07-09-2015/21:43:46	123.1	88.88	6.15E + 04	134	81.19	735.2
1832	08-09-2015/02:17:22	122.9	88.86	6.18E + 04	136.6	80.1	742.9
1833	08-09-2015/06:50:53	123.6	88.64	6.32E + 04	132.1	81.73	734.4
1834	08-09-2015/11:24:17	122.5	88.4	6.76E + 04	134.4	80.29	752.3
1835	08-09-2015/15:57:33	123	88.21	5.50E + 04	132.4	81.02	746
1836	08-09-2015/20:30:49	123.3	88.09	6.24E + 04	134.7	80.1	743.5
1837	09-09-2015/01:03:53	122.3	87.82	6.74E + 04	136.4	79.03	751.8

$$N_m = N_0 Ch^{-k} \tag{3}$$

calculating the best fit subsolar peak density  $N_0$  and the best fit value of the exponent  $k$ . The exponent  $k$  is theoretically predicted to be 0.5. *Hantsch and Bauer* [1990] showed that the electron densities measured from the early Mars missions could be fit with  $k = 0.57$ , and subsequent studies have found similar values ranging from 0.465 [*Fox and Yeager*, 2006] to 0.546 [*Němec et al.*, 2011].

We begin by examining the predicted dependence of the peak density and peak altitude on solar zenith angle. We follow the analysis of several other studies [e.g., *Fallows et al.*, 2015, and references therein] in fitting the observed peak densities and peak altitudes to similar equations and calculating the best fit parameters. Figure 4 (left) shows the peak density as a function of solar zenith angle, with colored lines corresponding to equation (3) using the best fit values from values of  $N_0$  and  $k$  calculated in several previous studies [*Fallows et al.*, 2015; *Fox and Yeager*, 2006; *Fox and Yeager*, 2009; *Hantsch and Bauer*, 1990; *Morgan et al.*, 2008; *Němec et al.*, 2011; *Nielsen et al.*, 2006]. Note that several studies performed the fit to  $N_m = N_0 \cos(\chi)^k$ , but here we use only the Chapman grazing function as in equation (3) for consistency. The behavior of the MAVEN peak densities with changes in solar zenith angle is broadly consistent with previous results, although the MAVEN peak densities are slightly smaller than predicted by all except *Morgan et al.* [2008] and *Němec et al.* [2011]. We applied equation (3) to the MAVEN peak densities and calculated the best fit  $N_0$  and  $k$  values by using a non-linear least squares fit; the results of our fit are shown in Figure 4 in black. We found a best fit  $N_0$  value of

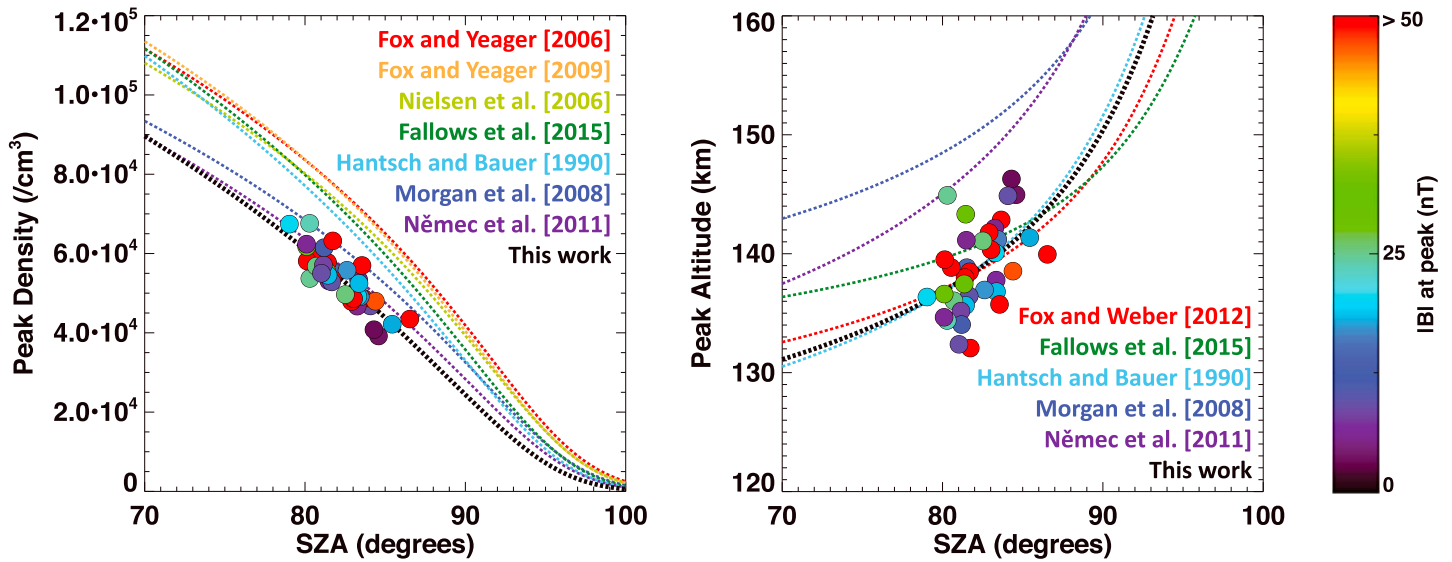


**Figure 4.** (left) Peak density as a function of solar zenith angle. The dot colors indicate the magnetic field magnitude at the peak altitude. The dashed lines correspond to equation (3) using the best fit values of  $N_0$  and  $k$  calculated in previous studies, with color indicating the work cited as noted by legend. The black line shows the best fit to the MAVEN data (see text). (right) Peak altitude as a function of solar zenith angle. Symbol colors indicate the magnetic field magnitude at the peak altitude. The dashed lines correspond to equation (2) using the best fit values of  $z_0$  and  $H$  calculated in previous studies, with color indicating the work cited as noted by the legend. The black line shows the best fit to the MAVEN data (see text).

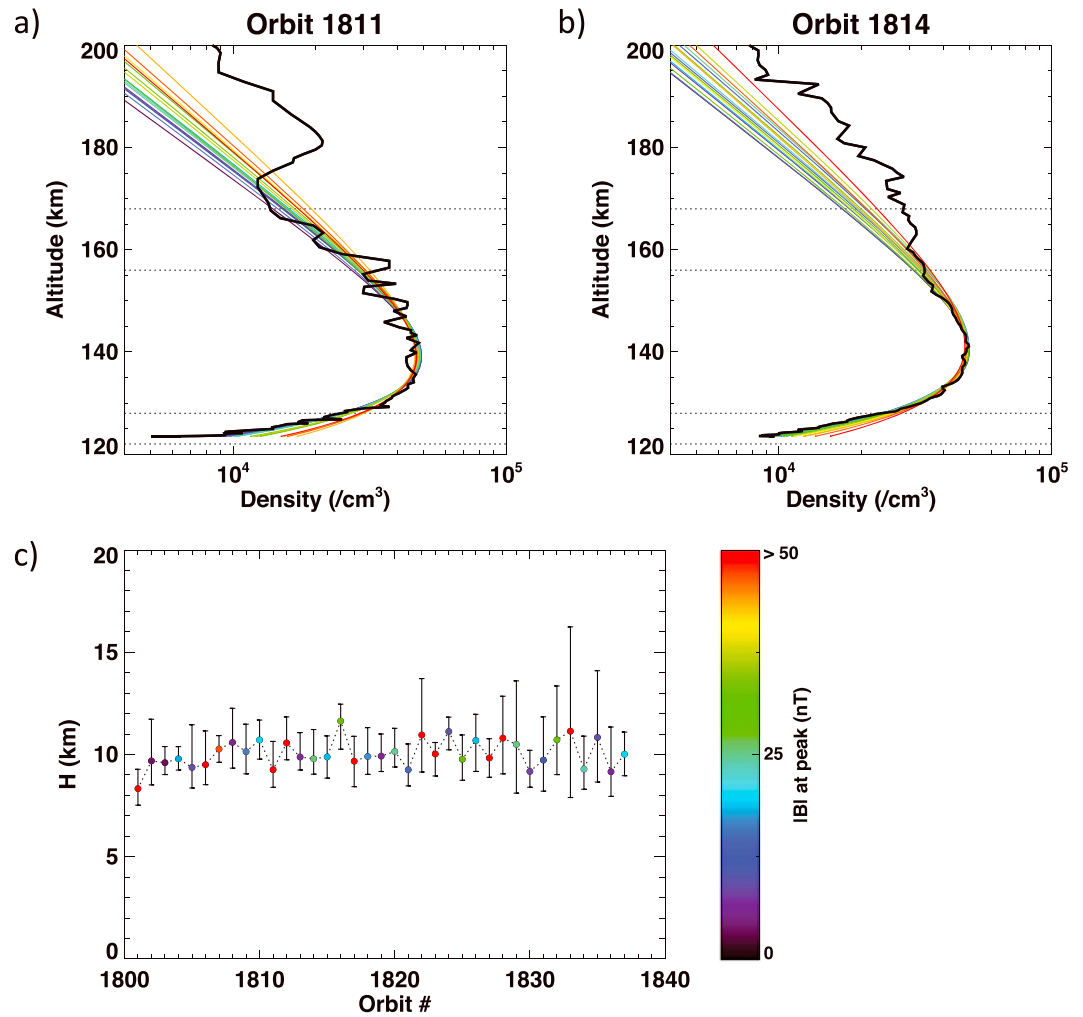
$(1.71 \pm 0.22) \times 10^5 \text{ cm}^{-3}$  and  $k = 0.62 \pm 0.07$ . Our results are roughly consistent with the best fit  $N_0$  and  $k$  values corresponding to the seven curves plotted in Figure 4 (see Table 1 of *Fallows et al.* [2015] for a complete list); those studies found that  $N_0$  varied from  $1.58 \times 10^5 \text{ cm}^{-3}$  [*Morgan et al.*, 2008] to  $1.97 \times 10^5 \text{ cm}^{-3}$  [*Fallows et al.*, 2015], and  $k$  varied from 0.465 [*Fox and Yeager*, 2006] to 0.57 [*Hantsch and Bauer*, 1990].

Figure 4 (right) shows the peak altitude as a function of solar zenith angle. Several previous studies have fit the peak altitude by using equation (2) or a form of equation (2) in which the Chapman grazing function is replaced with  $\sec(\chi)$ . These fits provide the best fit subsolar peak altitude  $z_0$  and neutral scale height  $H$ . The resulting best fit curves are shown by the colored curves in Figure 4 (right) [*Fallows et al.*, 2015; *Fox and Weber*, 2012; *Hantsch and Bauer*, 1990; *Morgan et al.*, 2008; *Němec et al.*, 2011]. We fit equation (2) to the 37 observed MAVEN peak altitudes and calculated the best fit  $z_0$  and  $H$  values by using a nonlinear least squares fit; the results of our fit are shown in black. We found a best fit  $z_0 = 121.5 \pm 5.5 \text{ km}$  and  $H = 9.1 \pm 2.9 \text{ km}$ . These values are consistent with the ranges of best fit  $z_0$  and  $H$  values from previous studies, 120–133.6 km for  $z_0$  [*Hantsch and Bauer*, 1990; *Morgan et al.*, 2008] and 5.2–12.2 km for  $H$  [*Fallows et al.*, 2015; *Němec et al.*, 2011]; see Table 2 of *Fallows et al.* [2015] for a complete list of the best fit parameters.

The neutral scale height  $H$ , which represents the vertical width of the main peak, can also be calculated from an individual electron density profile. In analytical photochemical theory, the electron density  $N$  is given by

$$N(z, Ch) = N_0 \exp\left(\frac{1}{2} \left(1 - \frac{z - z_0}{H} - Ch \exp\left(-\frac{z - z_0}{H}\right)\right)\right), \quad (4)$$

where  $z$  is altitude. We have applied equation (4) to each profile and calculated the best fit  $N_0$ ,  $z_0$ , and  $H$  for each profile by using a nonlinear least squares fit. The results of the fit are sensitive to the altitude range over which the fit is performed. In Figures 5a and 5b the various colored lines show different fits applied to data with a lower altitude limit ranging from 122 to 128 km and an upper altitude limit ranging from 156 to 168 km. For each orbit we fit the data to equation (4) over different altitude ranges, calculating several values of the best fit  $H$ . The circles in Figure 5c show the average of the best fit  $H$  values for each orbit, and the error bars show the range of the best fit  $H$  values for each orbit. In the case of orbit 1836, the best fit  $H$  ranges from 8.0 to 11.3 km, with an average of 9.2 km. For all 37 orbits the average best fit  $H$  values range from 8.3 to 11.6 km with an average of 10.0 km. *Ergun et al.* [2015] fit MAVEN LPW electron density profiles from the April 2015 deep dip interval to a Chapman function and found a best fit  $H$  of 12.6 km, roughly consistent with



**Figure 5.** (a) Electron density profile from orbit 1811 (black) with the best fit Chapman function from equation (4). The colored lines show different fits applied to data with a lower altitude limit ranging from 122 to 128 km and an upper altitude limit ranging from 156 to 168 km (horizontal dashed lines). (b) As in Figure 5a but for orbit 1814. (c) Best fit neutral scale height  $H$  as a function of orbit number. For each orbit, the fit was performed several times as shown in Figure 5a. The circles show the resulting average  $H$  fit for each orbit, with colors indicating the magnetic field magnitude at the peak altitude, and error bars show the range of the best fit  $H$  values for each orbit.

our results. The April 2015 deep dip profiles did not include the main peak because the orbital periapsis was  $\sim 130$  km and the peak altitude was  $\sim 124$  km as inferred from the fits.

There is not a significant difference in the average best fit  $H$  values for orbits with a strong crustal magnetic field and orbits without a strong crustal magnetic field. However, we do find that the orbits without a strong crustal magnetic field are the most well described by a smooth Chapman function near the peak, with the best agreement between the observed and best fit  $N_m$  values and the smallest root-mean-square error in the overall fit. An example of this can be seen in Figures 5a and 5b, which show the Chapman function fits for an orbit with (orbit 1811) and without (orbit 1814) strong crustal magnetic fields. The electron density profile from orbit 1814 is very smooth, and the peak electron density and peak altitude are well fit by the colored Chapman function lines. By comparison, the electron density from orbit 1811 is more ragged and the peak electron density is slightly lower, and the peak altitude is slightly higher, than predicted by the colored Chapman function fits.

Overall, we find that the best fit subsolar peak electron density,  $N_0$ , is consistent with the values obtained by previous studies. Our best fit exponent  $k$  in equation (3) is larger than the theoretical value, 0.5, predicted by Chapman theory and larger than the results found in previous studies. However, here we have analyzed only a few dozen data points that are clustered at a narrow range of large solar zenith angles, while other studies

have employed thousands of data points [e.g., *Morgan et al.*, 2008] from a larger range of solar zenith angles [e.g., *Hantsch and Bauer*, 1990]. Additionally, peak electron densities vary with Mars season and with the phase in solar cycle [*Withers et al.*, 2015a]. Finally, our best fit  $z_0$  and  $H$  are also consistent with previous studies. Differences between our results and those of previous studies may be partially explained by differences in the spatial coverage, season, and solar irradiance for the data sets under consideration.

### 3.3. Electron Temperatures at the Peak Altitude

Prior to MAVEN, the only electron temperatures measured in the Martian ionosphere came from a single profile from the Viking lander that did not include the altitude of the peak electron density [*Hanson and Mantas*, 1988]. For nearly three decades the Viking measurements, which extended only as low as  $\sim 200$  km, have provided the only observational constraint to models of electron temperatures in the Martian ionosphere [e.g., *Matta et al.*, 2014]. Electron temperatures influence the peak electron density because the rate at which  $O_2^+$  is lost through dissociative recombination varies inversely with the electron temperature. Analytical photochemical theory predicts that the peak density depends on the ionizing flux  $F$  as follows

$$N_m = \sqrt{\frac{F}{\alpha H e C h}}, \quad (5)$$

where  $\alpha$  is the  $O_2^+$  dissociative recombination coefficient and  $e$  is the base of the natural logarithm [*Withers*, 2009; *Girazian and Withers*, 2013]. Given  $\alpha = 2.4 \times 10^{-7} \left(\frac{300 \text{ K}}{T_e}\right)^{0.7} \text{ cm}^3 \text{ s}^{-1}$  for  $T_e < 1200 \text{ K}$  [*Schunk and Nagy*, 2009], equation (5) can be rewritten as

$$N_m = \sqrt{\frac{F}{2.4 \times 10^{-7} \left(\frac{300 \text{ K}}{T_e}\right)^{0.7} H e C h}}, \quad (6)$$

so that the largest peak electron densities are expected for highest electron temperatures if all other variables (solar ionizing flux, solar zenith angle) are held constant.

Figure 6a shows the MAVEN LPW electron temperatures at the peak altitudes for all 37 orbits from the September deep dip. The electron temperature profile from orbit 1824 shown in Figure 2 is a fairly typical example of the data set as a whole. The electron temperature at the peak, 741.9 K, is slightly below the average 764.2 K from all 37 orbits. Overall, the electron temperature at the peak varies from 728.7 to 822.4 K. The electron temperature appears to decrease slightly with orbit number, from  $\sim 800$  K to  $\sim 740$  K. This change is consistent with the decrease in the peak altitude from  $\sim 145$  km to  $\sim 135$  km caused by changes in solar zenith angle over the 37 orbits; in all 37 electron density profiles the average electron temperature is 801.9 K at 145 km altitude and 736.4 K at 135 km altitude.

Since the peak electron density increased over the 7 day interval, as shown in Figure 3a, the density and temperature are weakly anticorrelated (linear correlation coefficient  $-0.41$ ), which can be seen in Figure 6b. Despite this anticorrelation, the predicted peak electron densities calculated from equation (6) follow the observed peak electron densities very well, as shown in Figures 6c and 6d. We assume a constant solar ionizing flux of  $\sim 9.0 \times 10^{-4} \text{ W/m}^2$  and a constant scale height of 10 km, which is consistent with measured values [e.g., *Withers*, 2006], so that the predicted peak density is a function of solar zenith angle and electron temperature only. The resulting predicted peak electron densities are  $\sim 18\%$  larger than the observed values but are well correlated with the observed values (linear correlation coefficient 0.81) and both quantities show a similar trend with orbit number due to changes in the solar zenith angle over time. The overprediction is consistent with the result from section 3.2 that the peak density falls off with solar zenith angle more quickly than expected ( $N_m$  is proportional to  $Ch^{-0.62}$  instead of the predicted  $Ch^{-0.5}$ ).

Overall, we find that the observed variability in electron temperatures at the ionospheric peak is consistent with the observed variability in the peak electron density during this interval, specifically changes in the peak density with solar zenith angle over this interval. This suggests that the electron temperature at the main peak is dependent on solar zenith angle because the altitude of the peak electron density also depends on solar zenith angle. *Withers et al.* [2014] came to an opposite conclusion based on simulations of the dependence of the peak electron density with temperature using the Boston University ionosphere model [e.g.,

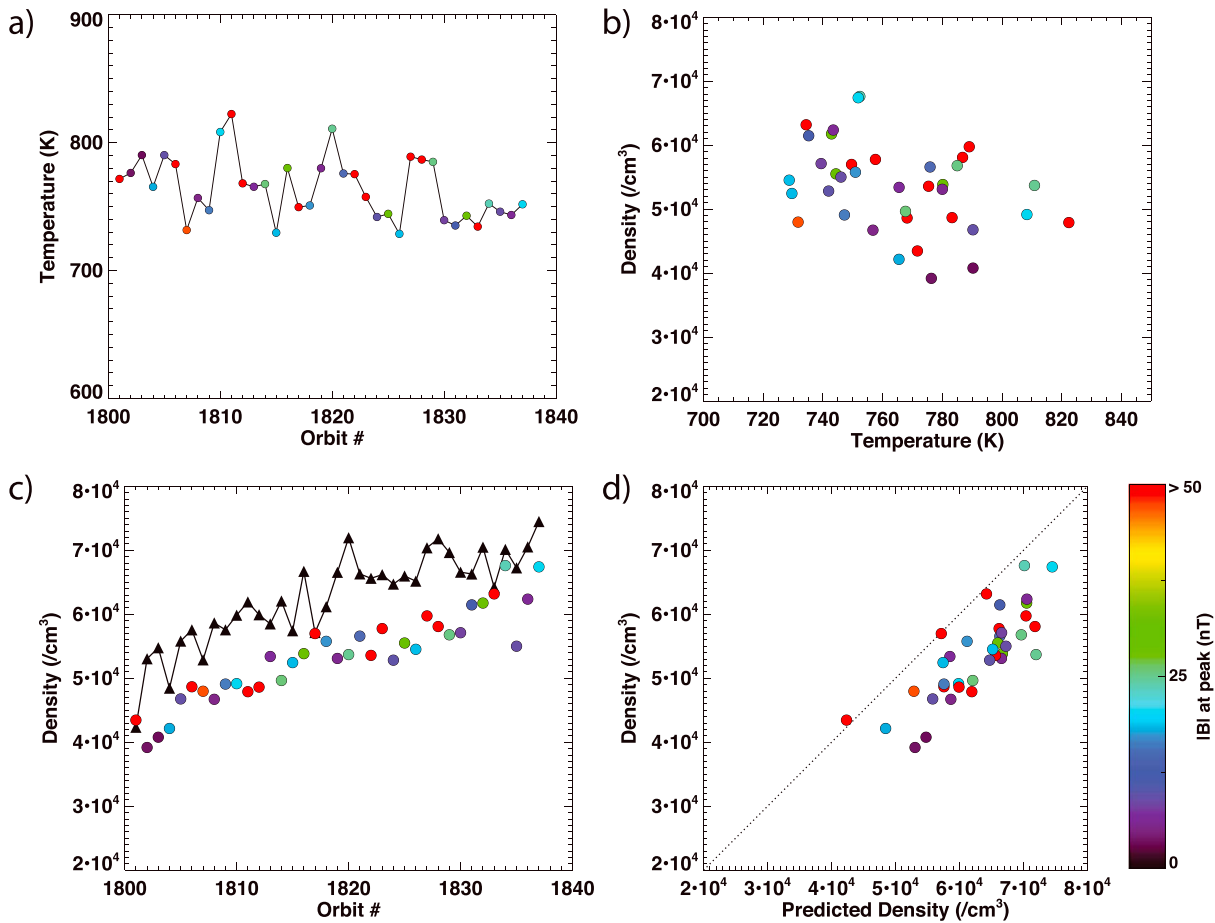


**Figure 6.** LPW electron temperature measurements at the peak altitude and predicted electron densities in the September 2015 deep dip interval. In all panels color indicates the magnetic field magnitude at the peak. (a) Temperature at the peak altitude as a function of orbit number. (b) Scatterplot of electron density as a function of temperature. (c) Peak electron density as a function of orbit number. Measured values are shown by the colored circles, and values predicted from equation (6) are shown by the black triangles (see text). (d) Measured peak electron densities as a function of predicted peak electron density.

*Martinis et al., 2003; Matta et al., 2013*]. However, they assumed an electron temperature profile based on extrapolations of the Viking lander measurements to lower altitudes [*Mendillo et al., 2011*]. They predicted temperatures of ~300–350 K at 145 km altitude and ~200–250 K at 135 km altitude, lower than those observed with MAVEN by about a factor of 2. The MAVEN electron temperatures also differ from the Viking measurements. Viking recorded a temperature of ~3350 K at 250 km altitude, while the average MAVEN electron temperature at 250 km altitude was 1750 K. A detailed analysis of these differences is beyond the scope of this study but will be crucial in applying Viking-based models to MAVEN data. Finally, we note that while the observed dependence of the electron temperature with solar zenith angle is consistent with changes in the peak altitude with solar zenith angle, the electron temperature at the main peak may also be dependent on solar zenith angle because the electron temperature depends on other factors not considered here, like the solar heating rate or neutral temperature, which can themselves be a function of solar zenith angle.

### 3.4. Composition of the Ionosphere and Neutral Atmosphere at the Peak Altitude

MAVEN data provide the first opportunity to study variability in the neutral and ion composition at the main ionospheric peak. In this section we examine variability in the NGIMS neutral and ion data at the peak altitude over the September 2015 deep dip interval. Figure 7a shows an example altitude profile of the various neutral species in the atmosphere during MAVEN orbit 1835. At the peak altitude, 132.4 km, the neutral atmosphere is 74.7% CO<sub>2</sub>, 14.2% O, 4.6% N<sub>2</sub>, 3.7% CO, 1.6% Ar, and 1.2% O<sub>2</sub>, with less than 1% of NO and He. Ion compositions at the peak altitude for orbit 1824 are presented in Figure 2a and discussed in section 3.1.

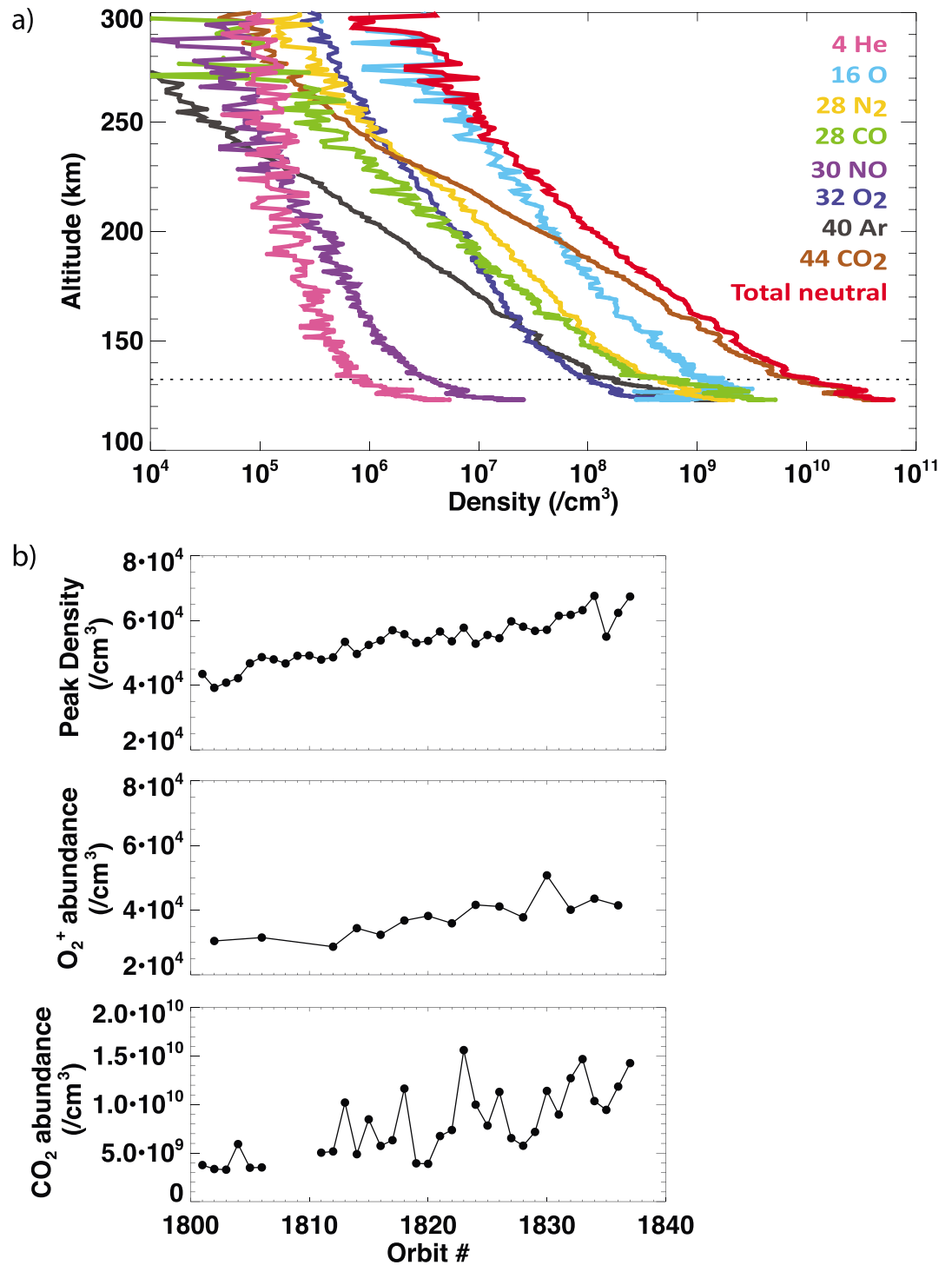


**Figure 7.** (a) NGIMS neutral density profiles from orbit 1835 inbound. The horizontal dashed line shows the altitude of the peak electron density measured by LPW. (b) Peak electron density (top),  $O_2^+$  (mass 32) ion density at the peak altitude (middle), and neutral  $CO_2$  (mass 44) density at the peak altitude (bottom) as a function of orbit number.

Figure 7b shows how the density of the most abundant ion,  $O_2^+$ , and most abundant neutral species,  $CO_2$ , at the peak altitude varies as a function of orbit number, while Figures 8a and 8c show how the fractional composition of various ion and neutral species at the peak altitude varies with orbit number. Simultaneous ion and neutral composition measurements are available every other orbit, when NGIMS operates in the open source ion mode.

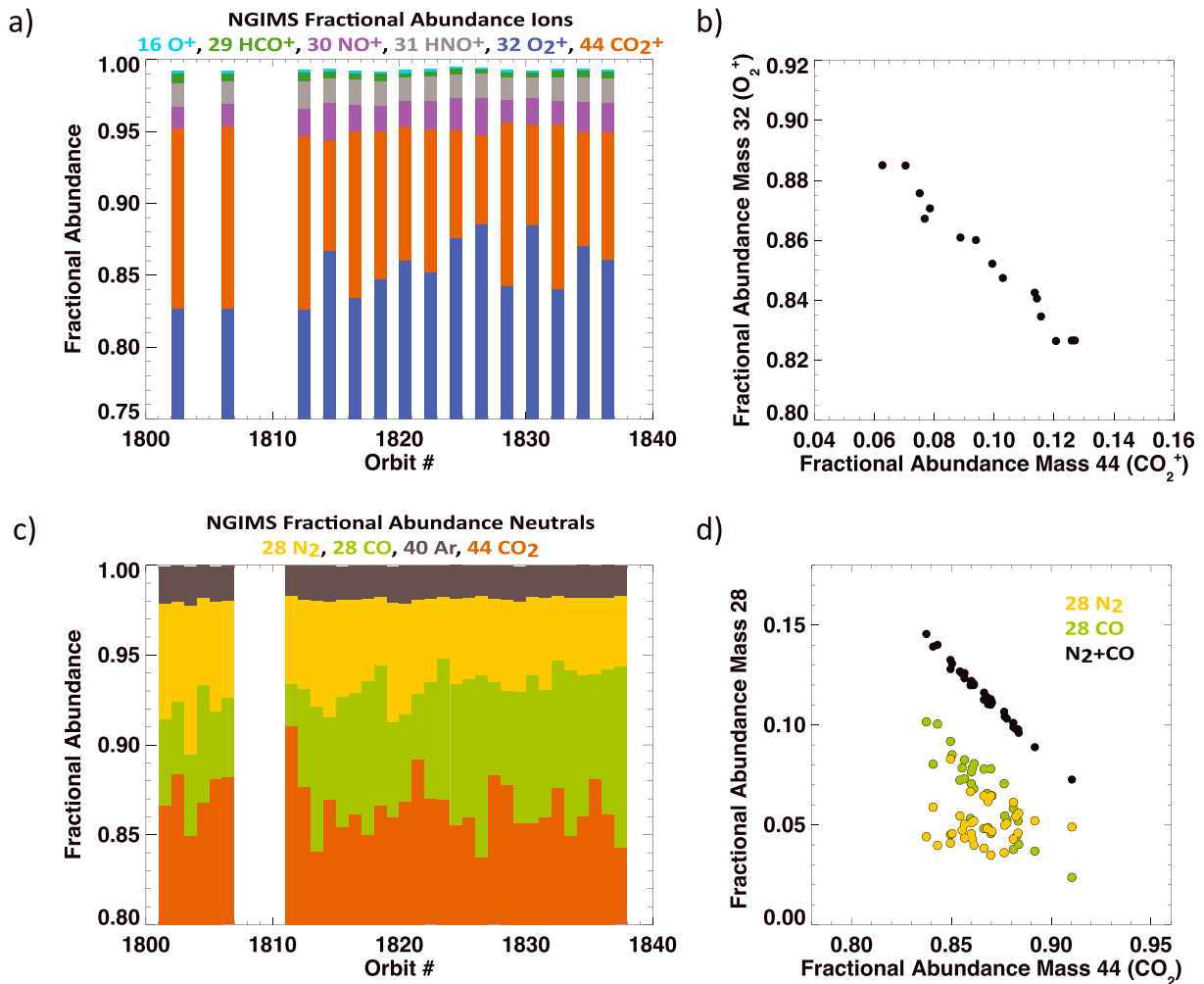


**Figure 8.** (a) Fractional abundance of different ion species as a function of orbit number. (b) Fractional abundance of O<sub>2</sub><sup>+</sup> (mass 32) as a function of the fractional abundance of CO<sub>2</sub><sup>+</sup> (mass 44). (c) Fractional abundance of different neutral species as a function of orbit number. In calculating the fractional abundance of each species we neglect mass 16 (O) and 32 (O<sub>2</sub>) in the total neutral abundance (see text). (d) Fractional abundance of N<sub>2</sub> (mass 28, yellow), CO (mass 28, green), and CO and N<sub>2</sub> together (black) as a function of the fractional abundance of neutral CO<sub>2</sub> (mass 44).

During alternate orbits, NGIMS operates in the open source neutral beaming mode and no ions are measured. While densities of all dominant neutral species can, in reality, be extracted from the data, neutral atomic and molecular oxygen measurements require additional processing due to a high instrumental background [Mahaffy *et al.*, 2014]. Therefore, when calculating the fractional abundance of each neutral species, as shown in Figure 8c, we neglect the contribution of O (mass 16) and O<sub>2</sub> (mass 32). The neutral atmosphere is expected to be ~2–5% O and ~1% O<sub>2</sub> at 140 km [e.g., Nier and McElroy, 1977; Fox, 2015].

The densities of O<sub>2</sub><sup>+</sup> and CO<sub>2</sub> at the peak altitude display a steady increase with orbit number, as can be seen in Figure 7b. These trends are similar to the steady increase in the peak electron density with orbit number, which is caused by changes in MAVEN's orbital geometry over this interval. The O<sub>2</sub><sup>+</sup> density exhibits an orbit-by-orbit variability that is roughly similar in magnitude to the orbit-by-orbit variability in the peak electron density, but the CO<sub>2</sub> density displays much larger fractional changes from one orbit to another than either O<sub>2</sub><sup>+</sup> or the peak electron density.

Figures 8a and 8c show that the most abundant ion at the peak altitude is O<sub>2</sub><sup>+</sup>, representing ~83–89% of the total, and the most abundant neutral species is CO<sub>2</sub>, representing ~84–91% of the total. The second most abundant ion is CO<sub>2</sub><sup>+</sup>, representing ~6–13% of the total, and the second and third most abundant neutral species are CO (mass 28) at ~2–10% of the total and N<sub>2</sub> (mass 28) at ~3–8% of the total. There is no systematic change of the relative ion

abundances with orbit number that would indicate a dependence on solar zenith angle. Over this interval there is a slight increase in the fractional abundance of CO and corresponding decrease in the fractional abundance of N<sub>2</sub>.

What is most striking in Figures 8a and 8c is that even though the fractional abundance of each individual ion and neutral species is quite variable, the fraction of the total represented by the sum of O<sub>2</sub><sup>+</sup> and CO<sub>2</sub><sup>+</sup> is remarkably steady at ~95%, and the fraction of the total represented by the three most abundant neutral species (CO<sub>2</sub>, CO, and N<sub>2</sub>) is remarkably steady at ~98%. For the neutral atmosphere, this means that the fractional abundance of Ar is a near-constant ~2%. The fractional abundances of O<sub>2</sub><sup>+</sup> and CO<sub>2</sub><sup>+</sup> are strongly anticorrelated, with a linear correlation coefficient of  $-0.988$ . Similarly, the fractional abundance of CO<sub>2</sub> and the sum of the fractional abundances of CO and N<sub>2</sub> have a linear correlation coefficient of  $-0.996$ . This can also be seen in Figure 8b, which shows the fractional abundance of O<sub>2</sub><sup>+</sup> as a function of the fractional abundance of CO<sub>2</sub><sup>+</sup>, and Figure 8c, which shows the fractional abundance of CO and N<sub>2</sub> as a function of the fractional abundance of CO<sub>2</sub>.

Most theoretical models predict that the ionospheric composition near the main peak is ~85% O<sub>2</sub><sup>+</sup> and ~10% O<sup>+</sup> [e.g., Withers *et al.*, 2015b], consistent with the NGIMS observations. However, these models do not predict the remarkable trend in the variability of the chemical composition of the ionosphere at the ionospheric peak [e.g., Matta *et al.*, 2013; Fox, 2015]. It implies that the chemistry of the most abundant ion species, O<sub>2</sub><sup>+</sup> and CO<sub>2</sub><sup>+</sup>, is decoupled from the chemistry of the other species, O<sup>+</sup>, HCO<sup>+</sup>, NO<sup>+</sup>, and HNO<sup>+</sup>. Future modeling work will be necessary to determine the implications of this observation for the chemical processes that occur within the ionosphere. Additionally, our findings have important implications for the applicability of analytical photochemical theory to the Martian ionosphere. Chapman theory assumes that the ionosphere consists of a single ion species (O<sub>2</sub><sup>+</sup>) that is produced by photoionization and lost via dissociative recombination. This assumption is mostly satisfied since O<sub>2</sub><sup>+</sup> is shown to be ~85% of the total ion density at the main peak, but we find changes in the ion composition at the peak, particularly in the fractional abundance of CO<sub>2</sub><sup>+</sup>, that cannot be accounted for by Chapman theory.

#### 4. Summary and Conclusions

MAVEN's September 2015 deep dip orbits provided the first opportunity to observe in situ the peak electron density in the Martian ionosphere since Viking. This deep dip interval included 37 orbits over 7 days in which the orbital periapsis was lowered to ~125 km. We have studied MAVEN data from this interval to examine conditions at the altitude of the main peak, including the electron density and temperature and the composition of the ionosphere and neutral atmosphere.

The peak densities increased from  $\sim 4 \times 10^4 \text{ cm}^{-3}$  to  $\sim 7 \times 10^4 \text{ cm}^{-3}$  and the peak altitudes increased from ~132 km to ~146 km as the spacecraft solar zenith angle increased over the 37 orbits. The electron temperatures also slightly decreased, from ~800 K to ~740 K. The variability in both the peak electron density and the peak altitude is broadly consistent with the trends predicted by analytical photochemical theory. We found that the dependence of the peak density with solar zenith angle is proportional to  $Ch^{-0.62}$ , which is only roughly similar to the expected dependence on  $Ch^{-0.5}$ . Electron temperatures at the peak altitude influence the peak density because the O<sub>2</sub><sup>+</sup> dissociative recombination coefficient is a function of the electron temperature. We found that trends in the electron temperature at the ionospheric peak were consistent with changes in the peak electron density and concluded that the electron temperatures at the main peak are dependent on solar zenith angle because the altitude of the peak electron density also depends on solar zenith angle.

After accounting for changes in solar zenith angle, the orbit-to-orbit variability in the peak density, as indicated by changes in the inferred subsolar peak density values, is ~30%. Previous studies have linked variability in the peak density to factors like crustal magnetic fields or temporal changes in the solar ionizing flux. However, the solar ionizing flux was very steady during this interval and we did not find a clear association between the crustal magnetic field magnitude and orbit-to-orbit changes in the peak density.

Finally, we examined the composition of the ionosphere and neutral atmosphere at the altitude of the main peak. The most abundant ion at the peak altitude is O<sub>2</sub><sup>+</sup>, representing ~81–90% of the total, followed by CO<sub>2</sub><sup>+</sup>, representing ~5–13% of the total. The most abundant neutral species is CO<sub>2</sub>, representing ~84–91% of the total, followed by CO at ~3–10% of the total and N<sub>2</sub> at ~3–8% of the total, although we have neglected O and O<sub>2</sub> in our analysis. Remarkably, although the fractional abundance of each ion and neutral species is

quite variable, together  $O_2^+$  and  $CO_2^+$  consistently account for 95% of the total ion density and  $CO_2$ ,  $N_2$ , and  $CO$  consistently account for 98% of the total neutral density.

**Appendix A: Spacecraft Trajectory Effects**

With the exception of the Viking lander data, measurements of the peak electron density in the Martian ionosphere have all come from remote observations, notably radio occultation profiles from Mars Global Surveyor and MARSIS radar sounding profiles from Mars Express. Such remote observations are useful because they can provide vertical profiles at a constant solar zenith angle. By comparison, the solar zenith angle at which data are collected changes within each MAVEN profile as shown in Figure 1a. Here we consider how changes

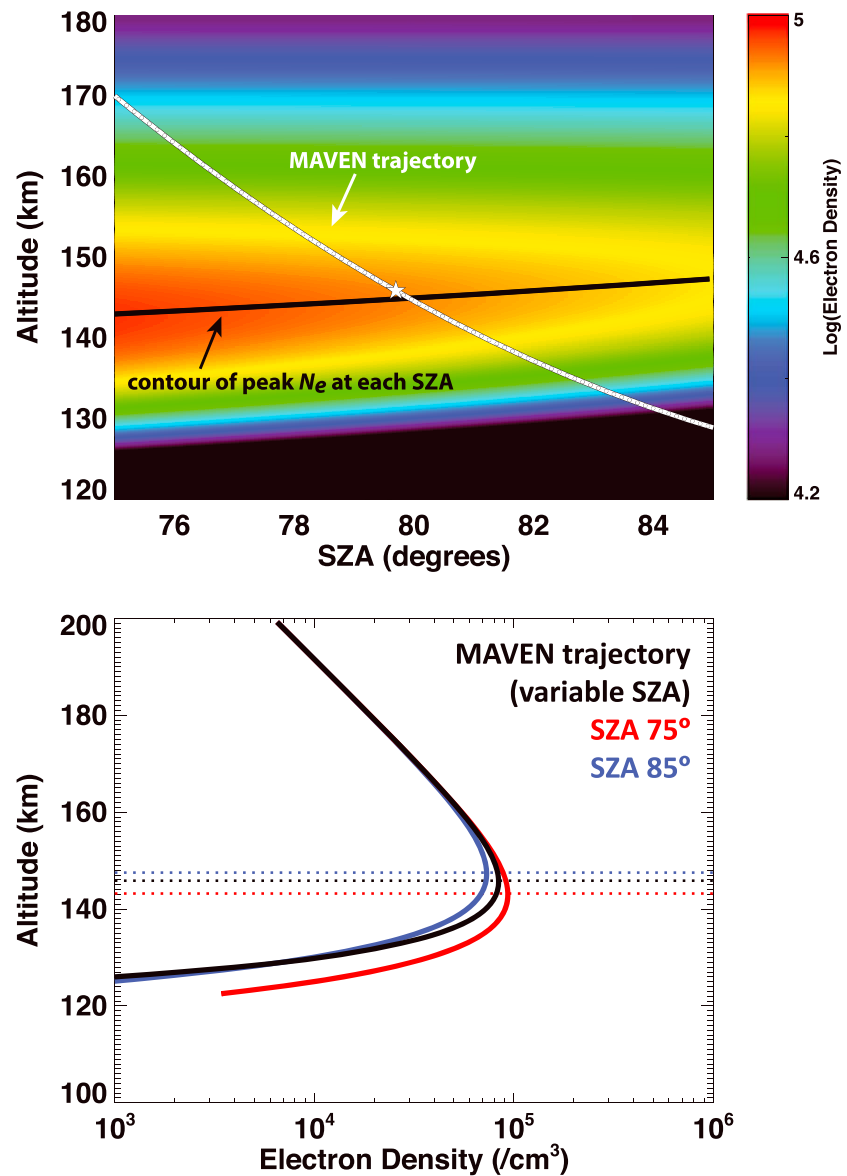


**Figure A1.** (top) MAVEN’s altitude as a function of solar zenith angle during the inbound portion of orbit 1821 (white line). The background color shows the electron densities predicted by a Chapman function (see text). The black line shows the model peak density at each solar zenith angle computed from the Chapman function. The star indicates the position of the peak model density observed along MAVEN’s trajectory. (bottom) Model density profile that would be observed along MAVEN’s trajectory during orbit 1821 (black). The model density profiles for a constant solar zenith angle of 75° and 85° are shown in red and blue, respectively. The horizontal dashed lines indicate the altitude of the peak density in each respective profile.

in solar zenith angle within a MAVEN electron density profile are expected to affect the observed peak density and its altitude.

Figure A1 (top) shows MAVEN's altitude as a function of solar zenith angle during the inbound portion of orbit 1821. The background color shows the electron densities predicted by a Chapman function following equation (4), with  $N_0 = 1.58 \times 10^5 \text{ cm}^{-3}$ ,  $z_0 = 133.6 \text{ km}$ , and  $H = 8.9 \text{ km}$ , as found by fits to MARSIS data from Mars Express [Morgan *et al.*, 2008]. The gray line shows the model peak density at each solar zenith angle computed from the Chapman function. If the spacecraft solar zenith angle were constant within an orbital pass MAVEN would record a peak in the electron density at a point along this gray line. However, because the spacecraft solar zenith angle changes with altitude, the model peak density observed along MAVEN's trajectory is located at the position marked by the white star. The peak density observed along MAVEN's trajectory is located  $\sim 1.1 \text{ km}$  higher in altitude and is 0.4% larger than what would be observed at a constant solar zenith angle  $80^\circ$ , which is roughly the solar zenith angle at which the spacecraft typically observed the peak density (see Table 1).

Figure A1 (bottom) shows the model density profile that would be observed along MAVEN's trajectory for orbit 1821 in black, along with the density that would be observed at constant solar zenith angles  $75^\circ$  in red and  $85^\circ$  in blue. The peak density observed along MAVEN's trajectory differs by about  $\sim 10\%$  compared to the peak densities in the red and blue curves, and the peak altitude differs by about  $\sim 3 \text{ km}$ . However, these differences are extreme examples, since MAVEN's solar zenith angle only varies by  $\sim 2^\circ$  within  $\sim 10 \text{ km}$  of the peak altitude, not  $\sim 5^\circ$  as in this example. Overall, we find that orbital effects introduce a typical error of  $\sim 3\text{--}7\%$  in the peak density and  $\sim 1 \text{ km}$  in the peak altitude.

#### Acknowledgments

M.V. and P.W. were supported by NASA grant NNX13AO35G. Solar wind proxies from MAVEN's SWIA instrument were kindly provided by Jasper Halekas. We thank two anonymous reviewers for their helpful suggestions. MAVEN data are available via the Planetary Plasma Interactions node of NASA's Planetary Data System at <http://ppi.pds.nasa.gov/>.

#### References

- Andersson, L., R. E. Ergun, G. T. Delory, A. Eriksson, J. Westfall, H. Reed, J. McCauly, D. Summers, and D. Meyers (2015), The Langmuir probe and waves (LPW) instrument for MAVEN, *Space Sci. Rev.*, doi:10.1007/s11214-015-0194-3.
- Cain, J. C., B. B. Ferguson, and D. Mozzoni (2003), An  $n = 90$  internal potential function of the Martian crustal magnetic field, *J. Geophys. Res.*, 108(E2), 5008, doi:10.1029/2000JE001487.
- Chamberlin, P. C., T. N. Woods, and F. G. Eparvier (2007), Flare Irradiance Spectral Model (FISM): Daily component algorithms and results, *Space Weather*, 5, S07005, doi:10.1029/2007SW000316.
- Chamberlin, P. C., T. N. Woods, and F. G. Eparvier (2008), Flare Irradiance Spectral Model (FISM): Flare component algorithms and results, *Space Weather*, 6, S05001, doi:10.1029/2007SW000372.
- Chapman, S. (1931a), The absorption and dissociative or ionizing effect of monochromatic radiation in an atmosphere on a rotating Earth, *Proc. Phys. Soc.*, 43, 26–45, doi:10.1088/0959-5309/43/1/305.
- Chapman, S. (1931b), The absorption and dissociative or ionizing effect of monochromatic radiation in an atmosphere on a rotating Earth. Part II. Grazing incidence, *Proc. Phys. Soc.*, 43, 483–501, doi:10.1088/0959-5309/43/5/302.
- Connerney, J. E. P., J. Espley, P. Lawton, S. Murphy, J. Odom, R. Oliverson, and D. Sheppard (2015), The MAVEN magnetic field investigation, *Space Sci. Rev.*, doi:10.1007/s11214-015-0169-4.
- Eparvier, F. G., P. C. Chamberlin, T. N. Woods, and E. M. B. Thiemann (2015), The solar extreme ultraviolet monitor for MAVEN, *Space Sci. Rev.*, 1–9, doi:10.1007/s11214-015-0195-2.
- Ergun, R. E., M. W. Morooka, L. A. Andersson, C. M. Fowler, G. T. Delory, D. J. Andrews, A. I. Eriksson, T. McEnulty, and B. M. Jakosky (2015), Dayside electron temperature and density profiles at Mars: First results from the MAVEN Langmuir probe and waves instrument, *Geophys. Res. Lett.*, 42, 8846–8853, doi:10.1002/2015GL065280.
- Fallows, K., P. Withers, and M. Matta (2015), An observational study of the influence of solar zenith angle on properties of the M1 layer of the Mars ionosphere, *J. Geophys. Res. Space Physics*, 120, 1299–1310, doi:10.1002/2014JA020750.
- Fox, J. L., and A. J. Weber (2012), MGS electron density profiles: Analysis and modeling of peak altitudes, *Icarus*, 221, 1002–1019, doi:10.1016/j.icarus.2012.10.002.
- Fox, J. L., and K. E. Yeager (2006), Morphology of the near-terminator Martian ionosphere: A comparison of models and data, *J. Geophys. Res.*, 111, A10309, doi:10.1029/2006JA011697.
- Fox, J. L., and K. E. Yeager (2009), MGS electron density profiles: Analysis of the peak magnitudes, *Icarus*, 200, 468–479, doi:10.1016/j.icarus.2008.12.002.
- Fox, J. L. (2015), The chemistry of protonated species in the martian ionosphere, *Icarus*, 252, 366–392, doi:10.1016/j.icarus.2015.01.010.
- Girazian, Z., and P. Withers (2013), The dependence of peak electron density in the ionosphere of Mars on solar irradiance, *Geophys. Res. Lett.*, 40, 1960–1964, doi:10.1002/grl.50344.
- Halekas, J. S., et al. (2015), MAVEN observations of solar wind hydrogen deposition in the atmosphere of Mars, *Geophys. Res. Lett.*, 42, 8901–8909, doi:10.1002/2015GL064693.
- Halekas, J. S., et al. (2016), Structure, dynamics, and seasonal variability of the Mars-solar wind interaction: MAVEN solar wind ion analyzer inflight performance and science results, *J. Geophys. Res. Space Physics*, 121, doi:10.1002/2016JA023167 in press.
- Hanson, W. B., and G. P. Mantas (1988), Viking electron temperature measurements: Evidence for a magnetic field in the Martian ionosphere, *J. Geophys. Res.*, 93(A7), 7538–7544, doi:10.1029/JA093iA07p07538.
- Hanson, W. B., S. Sanatani, and D. R. Zuccaro (1977), The Martian ionosphere as observed by the Viking retarding potential analyzers, *J. Geophys. Res.*, 82(28), 4351–4363, doi:10.1029/JS082i028p04351.
- Hantsch, M. H., and S. J. Bauer (1990), Solar control of the Mars ionosphere, *Planet. Space Sci.*, 38, 539–542, doi:10.1016/0032-0633(90)90146-H.
- Jakosky, B. M., et al. (2015), The Mars Atmosphere and Volatile Evolution (MAVEN) mission, *Space Sci. Rev.*, doi:10.1007/s11214-015-0139-x.

- Mahaffy, P. R., et al. (2014), The neutral gas and ion mass spectrometer on the Mars atmosphere and volatile evolution mission, *Space Sci. Rev.*, *195*(1), 49–73, doi:10.1007/s11214-014-0091-1.
- Martinis, C. R., J. K. Wilson, and M. J. Mendillo (2003), Modeling day-to-day ionospheric variability on Mars, *J. Geophys. Res.*, *108*(A10), 1383, doi:10.1029/2003JA009973.
- Matta, M., P. Withers, and M. Mendillo (2013), The composition of Mars' topside ionosphere: Effects of hydrogen, *J. Geophys. Res. Space Physics*, *118*, 2681–2693, doi:10.1002/jgra.50104.
- Matta, M., M. Galand, L. Moore, M. Mendillo, and P. Withers (2014), Numerical simulations of ion and electron temperatures in the ionosphere of Mars: Multiple ions and diurnal variations, *Icarus*, *227*, 78–88, doi:10.1016/j.icarus.2013.09.006.
- Mendillo, M., A. Lollo, P. Withers, M. Matta, M. Pätzold, and S. Tellmann (2011), Modeling Mars' ionosphere with constraints from same-day observations by Mars Global Surveyor and Mars Express, *J. Geophys. Res.*, *116*, A11303, doi:10.1029/2011JA016865.
- Morgan, D. D., D. A. Gurnett, D. L. Kirchner, J. L. Fox, E. Nielsen, and J. J. Plaut (2008), Variation of the Martian ionospheric electron density from Mars Express radar soundings, *J. Geophys. Res.*, *113*, A09303, doi:10.1029/2008JA013313.
- Němec, F., D. D. Morgan, D. A. Gurnett, F. Duru, and V. Truhlík (2011), Dayside ionosphere of Mars: Empirical model based on data from the MARSIS instrument, *J. Geophys. Res.*, *116*, E07003, doi:10.1029/2010JE003789.
- Nielsen, E., H. Zou, D. A. Gurnett, D. L. Kirchner, D. D. Morgan, R. Huff, R. Orosei, A. Safaieinili, J. J. Plaut, and G. Picardi (2006), Observations of vertical reflections from the topside Martian ionosphere, *Space Sci. Rev.*, *126*, 373–388, doi:10.1007/s11214-006-9113-y.
- Nielsen, E., et al. (2007), Local plasma processes and enhanced electron densities in the lower ionosphere in magnetic cusp regions on Mars, *Planet. Space Sci.*, *55*, 2164–217, doi:10.1016/j.pss.2007.07.003.
- Nier, A. O., and M. B. McElroy (1977), Composition and structure of Mars' Upper atmosphere: Results from the neutral mass spectrometers on Viking 1 and 2, *J. Geophys. Res.*, *82*(28), 4341–4349, doi:10.1029/JS082i028p04341.
- Rishbeth, H., and M. Mendillo (2004), Ionospheric layers of Mars and Earth, *Planet. Space Sci.*, *52*, 849–852, doi:10.1016/j.pss.2004.02.007.
- Schunk, R. W., and A. F. Nagy (2009), *Ionospheres*, 2nd ed., Cambridge Univ. Press, New York.
- Smith, F. L., and C. Smith (1972), Numerical evaluation of Chapman's grazing incidence integral  $Ch(X, \chi)$ , *J. Geophys. Res.*, *77*, 3592–3597, doi:10.1029/JA077i019p03592.
- Trotignon, J. G., C. Mazelle, C. Bertucci, and M. H. Acuña (2006), Martian shock and magnetic pile-up boundary positions and shapes determined from the Phobos 2 and Mars Global Surveyor data sets, *Planet. Space Sci.*, *54*, 357–369, doi:10.1016/j.pss.2006.01.003.
- Vignes, D., C. Mazelle, H. Reme, M. H. Acuña, J. E. P. Connerney, R. P. Lin, D. L. Mitchell, P. Cloutier, D. H. Crider, and N. F. Ness (2000), The solar wind interaction with Mars: Locations and shapes of the bow shock and magnetic pile-up boundary from the observations of the MAG/ER experiment onboard Mars Global Surveyor, *Geophys. Res. Lett.*, *27*, 49–52, doi:10.1029/1999GL010703.
- Withers, P. (2006), Mars Global Surveyor and Mars Odyssey Accelerometer observations of the Martian upper atmosphere during aerobraking, *Geophys. Res. Lett.*, *33*, L02201, doi:10.1029/2005GL024447.
- Withers, P. (2009), A review of observed variability in the dayside ionosphere of Mars, *Adv. Space Res.*, *44*, 277–307, doi:10.1016/j.asr.2009.04.027.
- Withers, P., and M. Mendillo (2005), Response of peak electron densities in the Martian ionosphere to day-to-day changes in solar flux due to solar rotation, *Planet. Space Sci.*, *53*, 1401–1418, doi:10.1016/j.pss.2005.07.010.
- Withers, P., K. Fallows, and M. Matta (2014), Predictions of electron temperatures in the Mars ionosphere and their effects on electron densities, *Geophys. Res. Lett.*, *41*, 2681–2686, doi:10.1002/2014GL059683.
- Withers, P., D. D. Morgan, and D. A. Gurnett (2015a), Variations in peak electron densities in the ionosphere of Mars over a full solar cycle, *Icarus*, *251*, 5–11, doi:10.1016/j.icarus.2014.08.008.
- Withers, P., et al. (2015b), Comparison of model predictions for the composition of the ionosphere of Mars to MAVEN NGIMS data, *Geophys. Res. Lett.*, *42*, 8966–8976, doi:10.1002/2015GL065205.